

Spin-Current-Controlled Modulation of the Magnon Spin Conductance in a Three-Terminal Magnon Transistor

L. J. Cornelissen,^{*} J. Liu, and B. J. van Wees

Physics of Nanodevices, Zernike Institute for Advanced Materials, University of Groningen, Nijenborgh 4, 9747 AG Groningen, The Netherlands

R. A. Duine

*Institute for Theoretical Physics and Center for Extreme Matter and Emergent Phenomena, Utrecht University, Leuvenlaan 4, 3584 CE Utrecht, The Netherlands
and Department of Applied Physics, Eindhoven University of Technology, P.O. Box 513, 5600 MB Eindhoven, The Netherlands*

 (Received 17 October 2017; published 2 March 2018)

Efficient manipulation of magnon spin transport is crucial for developing magnon-based spintronic devices. In this Letter, we provide proof of principle of a method for modulating the diffusive transport of thermal magnons in an yttrium iron garnet channel between injector and detector contacts. The magnon spin conductance of the channel is altered by increasing or decreasing the magnon chemical potential via spin Hall injection of magnons by a third modulator electrode. We obtain a modulation efficiency of 1.6%/mA at $T = 250$ K. Finite element modeling shows that this could be increased to well above 10%/mA by reducing the thickness of the channel, providing interesting prospects for the development of thermal-magnon-based logic circuits.

DOI: [10.1103/PhysRevLett.120.097702](https://doi.org/10.1103/PhysRevLett.120.097702)

In a field effect transistor (FET), the conductance of a semiconducting channel can be tuned by changing the density of charge carriers via the application of an electric field [1]. The FET proved to be an extremely powerful device for both signal amplification and logic operation and has become ubiquitous in present day electronics. Recently, the prospect of encoding, transporting, and manipulating information in solid-state devices based on magnons has sparked an intense research effort in the field of magnonics [2–4]. However, the task of manipulating information carried by magnons remains formidable.

On the one hand, low-frequency magnons propagating coherently are appealing, since they allow for on-chip access to wave phenomena like interference [5–7]. On the other hand, incoherent high-frequency thermal magnons propagating diffusively are promising, since they can be effectively interfaced with conventional electronics and are high-fidelity carriers of spin [8]. To develop magnon-based spintronic devices, efficient manipulation of magnon transport is crucial. Here we show that the magnon spin conductance of a magnetic insulator film can be tuned by changing the magnon density in that film, demonstrating an operating principle similar to the FET for electronic transport.

Thermal magnons can be excited and detected in the linear regime via spin-flip scattering of conduction electrons at a heavy metal|magnetic insulator interface [8–12]. They can also be excited by applying a thermal gradient to the magnet via the spin Seebeck effect (SSE) [13]. The SSE

drives a magnon spin current in response to the thermal gradient, which generates a voltage in an adjacent heavy metal layer and can be detected both in a local [13–17] or nonlocal [18–21] configuration. Manipulation of coherent magnon transport can be achieved, for instance, in magnonic crystals [22], which was used to realize the first magnon transistor [23]. Alternatively, damping compensation via spin transfer torque can be used to manipulate coherent magnon propagation [24–27]. Methods for the manipulation of thermal-magnon spin transport have not been demonstrated to date.

Ganzhorn *et al.* reported a linear superposition of magnon spin signals in a multiterminal injection and detection device [28]. Here we go beyond the linear regime to provide proof of principle for the manipulation of thermal-magnon transport by tuning the magnon spin conductivity σ_m in a three-terminal device on yttrium iron garnet (YIG). Similar to electron transport in metals and semiconductors, the conductance of a magnon channel depends on the magnon density. For electrons, this is captured in the Drude formula for the conductivity [29,30], $\sigma_e = e^2 n_e \tau_e / m_e$. Here, n_e is the free-electron density, $-e, m_e$ the electron charge and effective mass, and τ_e the scattering time. For magnons in thermal equilibrium, the spin conductivity (in units of 1/m) is [19]

$$\sigma_m = 4\zeta(3/2)^2 \frac{1}{\hbar} \frac{J_s \tau_m}{\Lambda^3}, \quad (1)$$

where J_s is the spin wave stiffness, Λ the thermal magnon de Broglie wavelength, τ_m the total momentum scattering time, ζ the Riemann zeta function, and \hbar the reduced Planck constant. For an out-of-equilibrium magnon gas, the density is no longer given by $n_m = 2\zeta(3/2)^2/\Lambda^3$ but depends on both chemical potential and temperature so that $n_m = n_m(\mu_m, T)$. For a parabolic dispersion $\hbar\omega = J_s k^2$, the effective mass is $m_m = \hbar^2/(2J_s)$. Thus, the out-of-equilibrium magnon spin conductivity becomes

$$\sigma_m = \hbar \frac{n_m \tau_m}{m_m}, \quad (2)$$

which is similar to the Drude formula and shows that σ_m can be tuned via the magnon density n_m .

The devices were fabricated on 210 nm thin YIG (111) films grown epitaxially on a gadolinium gallium garnet substrate. Three platinum electrodes are sputtered on top: an injector, modulator, and detector contact. The injector and detector have a width of 100 nm, and the modulator width is 1 μm . The center-to-center injector or detector distance is 1.5 μm , and the edge-to-edge distance between the modulator and side contacts is 200 nm. Three devices with different length and thickness of the Pt contacts were studied. For samples *G1* and *G3*, the contact length $l_{\text{pt}} = 12.5 \mu\text{m}$ and thickness $t_{\text{pt}} \approx 7 \text{ nm}$, whereas for sample *G2*, this is 100 μm and 10 nm, respectively. The electrodes are contacted by Ti/Au leads to make electrical connections to the device. A SEM image of device *G1* is shown in Fig. 1(a), with current and voltage connections indicated schematically. Nonlocal measurements are carried out by rotating the sample in a magnetic field H to vary the angle α between the Pt electrodes and the YIG magnetization (see the Supplemental Material [31], Sec. S8 for magnetization characteristics). A low-frequency $[\omega/(2\pi) < 20 \text{ Hz}]$ ac current is applied to the injector, while the first ($V^{1\omega}$)

and second ($V^{2\omega}$) harmonic response voltages are measured at the detector. All data shown in the main text of this manuscript were obtained from device *G1*, and the results for devices *G2* and *G3* are presented in the Supplemental Material [31]. All devices were fabricated on YIG samples cut from the same wafer.

$V^{1\omega}$ is due to magnons generated electrically via the spin Hall effect (SHE) in the injector and s - d exchange interaction at the Pt|YIG interface. $V^{2\omega}$ is due to thermally generated magnons excited via the SSE in response to the thermal gradient in the YIG arising from injector Joule heating. The detector signal arises from interfacial exchange interaction at the detector|YIG interface and the inverse SHE in the detector, for both $V^{1\omega}$ and $V^{2\omega}$. In addition to the ac current through the injector, we pass a dc current through the modulator. This influences the magnon transport channel in two ways. First, the average device temperature increases due to Joule heating in the modulator, altering the spin transport parameters. Second, magnons are injected or absorbed at the modulator|YIG interface, again relying on the SHE and interfacial spin-flip scattering. Depending on the relative orientation of the YIG magnetization and the spin accumulation in the modulator, this will increase or decrease the magnon density in the channel. The dc current will *not* simply result in a dc offset to $V^{1\omega}$ and $V^{2\omega}$ due to the lock-in method we employ (Supplemental Material [31], Sec. S5).

The nonlocal voltages are now [8]

$$V^{1\omega} = C_1 I_{\text{ac}} \sigma_m^{1\omega}(\alpha) \sin^2(\alpha + \phi^{1\omega}), \quad (3)$$

$$V^{2\omega} = C_2 I_{\text{ac}}^2 \sigma_m^{2\omega}(\alpha) \sin(\alpha + \phi^{2\omega}). \quad (4)$$

Here, I_{ac} is the ac injector current, $\phi^{1\omega}$ ($\phi^{2\omega}$) are offset angles in the first (second) harmonic, and the constants C_1

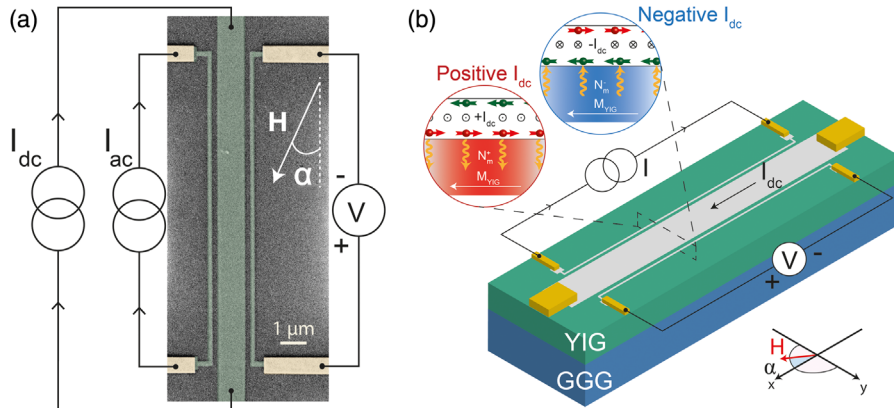


FIG. 1. (a) Colorized SEM image of device *G1*; electrical connections indicated schematically. Arrows mark charge current flow in the circuit. (b) A sketch of the device with schematic side views of the modulator|YIG interface for positive (negative) dc currents. When the magnetic moment of the spin accumulation μ_s in the modulator is antiparallel (parallel) to the YIG magnetization M_{YIG} , μ_m , and, hence, n_m in the channel is increased (decreased). Consequently, the magnon spin conductance from injector to detector is increased (decreased).

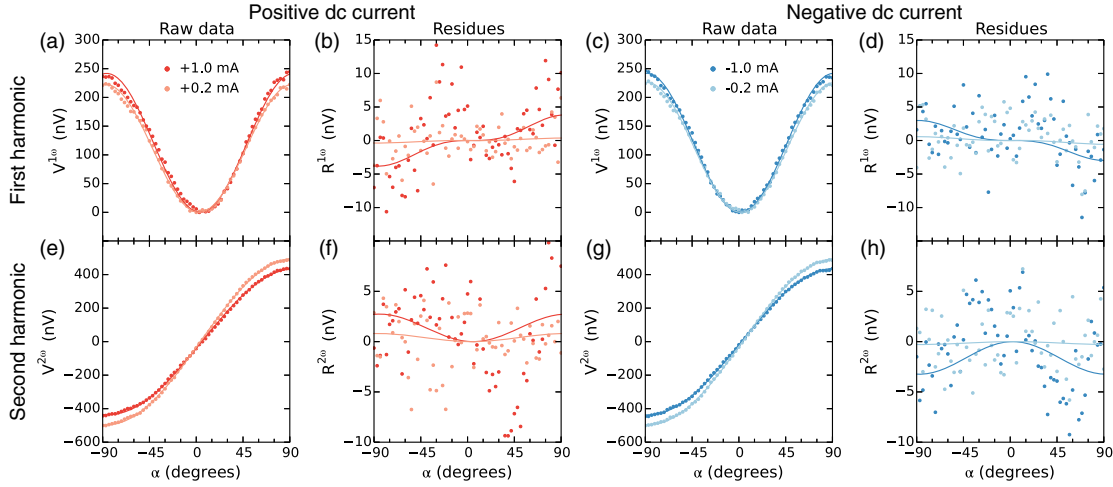


FIG. 2. (a),(b),(e),(f) [(c),(d),(g),(h)] First and second harmonic voltage for a positive (negative) dc modulator current as a function of α . Raw data are presented in (a) and (c) for the first harmonic; solid lines are $\sin^2(\alpha + \phi^{1\omega})$ fits to the data. For the second harmonic, (e) and (g) show the raw data fitted by a $\sin(\alpha + \phi^{2\omega})$ dependence. Panels (b),(d) [(f),(h)] show the residues (i.e., the data minus the fit) of the first (second) harmonic signal for positive and negative dc current, respectively. Residues are fitted by a $\sin^3(\alpha + \phi^{1\omega})$ and $\sin^2(\alpha + \phi^{2\omega})$ angular dependence for the first and second harmonic (solid lines). Residues for $I_{dc} = 0$ have been subtracted from the data to exclude effects not induced by the dc current. In (a) and (c), a constant offset was subtracted (see the Supplemental Material [31], Sec. S6). Data obtained for $I_{ac} = 100 \mu\text{A}$.

and C_2 capture the conversions from charge to magnon spin current and back, for electrical and thermal injection. The conductivity is

$$\sigma_m^{1\omega(2\omega)}(\alpha) = \sigma_m^0 + \Delta\sigma_J I_{dc}^2 + \Delta\sigma_{\text{SHE}} I_{dc} \sin(\alpha + \phi^{1\omega(2\omega)}), \quad (5)$$

where I_{dc} is the dc modulator current, σ_m^0 the spin conductivity of the channel without dc current, and $\Delta\sigma_J$ and $\Delta\sigma_{\text{SHE}}$ parametrize the efficiency of modulation via Joule heating and spin Hall injection of magnons, respectively. The angular dependence in the SHE term arises from the projection of the spin accumulation in the modulator on the YIG magnetization, which determines the efficiency of the magnon injection. The offset angles $\phi^{1\omega}$ and $\phi^{2\omega}$ can result from imperfect alignment of the sample in the magnetic field and are expected to be equal so that $\sigma_m^{1\omega}$ and $\sigma_m^{2\omega}$ are the same. Plugging Eq. (5) into Eqs. (3) and (4) gives

$$V^{1\omega} = A^{1\omega} \sin^2(\alpha + \phi^{1\omega}) + B^{1\omega} \sin^3(\alpha + \phi^{1\omega}), \quad (6)$$

$$V^{2\omega} = A^{2\omega} \sin(\alpha + \phi^{2\omega}) + B^{2\omega} \sin^2(\alpha + \phi^{2\omega}), \quad (7)$$

showing that modulator heating affects the amplitude of the nonlocal voltages (the A parameters), whereas injection of magnons via SHE modifies the angular dependence of the signals (the B parameters). Consequently, $A \propto I_{dc}^2$ and $B \propto I_{dc}$.

Figure 2 shows nonlocal measurement results as a function of the angle for positive [Figs. 2(a), 2(b), 2(e), and 2(f)] and negative [Figs. 2(c), 2(d), 2(g), and 2(h)] dc

currents and for the first (top row) and second (bottom row) harmonic, at $T = 250 \text{ K}$. The raw data are presented in Figs. 2(a) and 2(c) [Figs. 2(e) and 2(g)] for the first (second) harmonic and are fitted using the first terms in Eq. (6) [Eq. (7)] to find the amplitude $A^{1\omega}$ ($A^{2\omega}$) and phase $\phi^{1\omega}$ ($\phi^{2\omega}$). Then, the residues of the fits are calculated (i.e., the data minus the fitted curve), which are shown in Figs. 2(b) and 2(f) [Figs. 2(d) and 2(h)] and fitted using the last term in Eq. (6) [Eq. (7)] to find the amplitude $B^{1\omega}$ ($B^{2\omega}$). This procedure was repeated as a function of I_{dc} to identify the current dependence of A and B .

Figures 3(a) and 3(c) show the fit results for $A^{1\omega}$ and $A^{2\omega}$, from which the quadratic dependence on I_{dc} can be seen. The sign of the current dependence for $A^{1\omega}$ and $A^{2\omega}$ is opposite because the temperature dependence of electrically and thermally generated magnon signals has opposite sign [37]. We performed thermal modeling to estimate the temperature increase due to the injected dc current and found that this can be up to 50 K for $I_{dc} = 1 \text{ mA}$, depending on the sample temperature. Such a channel temperature increase can approximately explain the amplitude change in both first and second harmonic at $T = 250 \text{ K}$ (Supplemental Material [31], Sec. S2). For lower temperatures, the first harmonic modulation is larger than expected from the modeling. Figures 3(b) and 3(d) show the fit results for $B^{1\omega}$ and $B^{2\omega}$, which depend linearly on I_{dc} as expected. The slope dB/dI_{dc} of the B vs I_{dc} curves gives the efficiency of the modulation by SHE injection of magnons. At $T = 250 \text{ K}$, we find $dB^{1\omega}/dI_{dc} = 3.3 \pm 0.2 \text{ nV/mA}$ and $dB^{2\omega}/dI_{dc} = 3.3 \pm 0.3 \text{ nV/mA}$, with the relative modulation efficiency

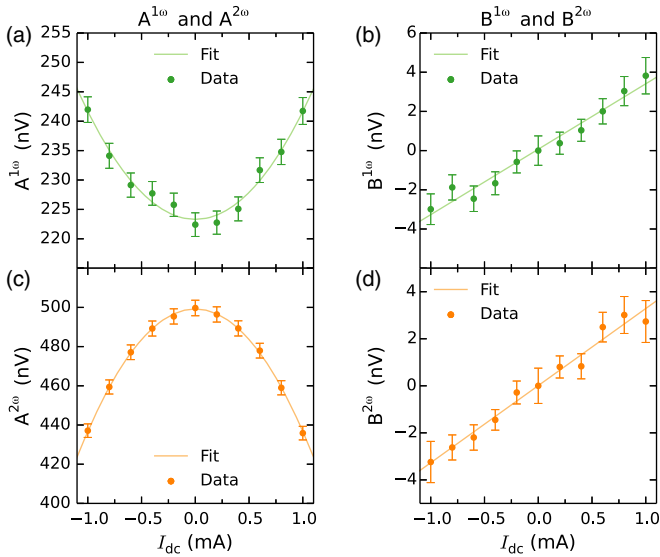


FIG. 3. (a) [(c)] Amplitude of the $\sin^2 \alpha$ oscillation ($\sin \alpha$) as a function of dc current. Solid lines are quadratic fits to the data. (b),(d) The amplitudes of the $\sin^3 \alpha$ and $\sin^2 \alpha$ component in the first and second harmonic voltage, respectively. Solid lines are linear fits to the data. Data obtained at $T = 250$ K. Error bars represent one standard error obtained from the least squares fits to Eqs. (6) and (7).

$$\eta = \frac{dB/dI_{dc}}{A_0}, \quad (8)$$

where $A_0 = A(I_{dc} = 0)$. We find $\eta = 1.6\%/mA$ ($0.7\%/mA$) for the first (second) harmonic. The sign of dB/dI_{dc} is consistent with the mechanism sketched in Fig. 1(b), which assumes a positive spin Hall angle in platinum [38] for all measurements on sample *G1*. This is also consistent with the sign of the thermally generated voltage: For the injector-detector distance measured here, the detector probes magnon accumulation [39], which results in a positive voltage for positive angles [Fig. 2(e)] in the measurement configuration of Fig. 1(a). For a positive dc current and positive angles, a positive voltage is observed in the residues for the first harmonic [Fig. 2(b)], meaning that the number of magnons in the channel is indeed increased by the positive current in this configuration.

On samples *G2* and *G3*, however, we observed a sign change of dB/dI_{dc} in the first harmonic as a function of the external magnetic field, which is unexpected and presently not understood (Supplemental Material [31], Sec. S1). The offset angles $\phi^{1\omega}$ and $\phi^{2\omega}$ also showed a dependence on the current, discussed in the Supplemental Material [31], Sec. S3.

The modulation efficiency can be estimated using a finite element model of our devices (see Supplemental Material [31], Sec. S4 for details). The magnon chemical potential profile due to the dc current injection is shown in Fig. 4(a). A large portion of the magnons is absorbed by the injector and detector contacts next to the modulator. Subsequently,

we calculate the average chemical potential in the channel induced by the dc current, μ_m^{dc} . This is plotted in Fig. 4(b) as a function of the current for $T = 250$ K.

The number of magnons in the YIG is given by

$$N = \int_{E_Z}^{\infty} D(\epsilon) f(\mu, T, \epsilon) d\epsilon, \quad (9)$$

with $E_Z = g\mu_B H_t$ the Zeeman energy, $D = 1/(4\pi^2) J_s^{3/2} \sqrt{\epsilon - g\mu_B H_t}$ the magnon density of states, and $f = (\exp\{[(\epsilon - \mu_m)/(k_B T)]\} - 1)^{-1}$ the Bose-Einstein distribution. $H_t = \sqrt{H(H + M_s)}$ is the total internal magnetic field in the film (for in-plane H). Assuming the magnon momentum scattering time to be weakly dependent on magnon density, we have from Eq. (2), $\Delta N/N_0 = \Delta\sigma_m/\sigma_m^0$, where N_0 and σ_m^0 are the number of magnons and magnon spin conductivity in the absence of a dc current. The low-energy part of the magnon distribution is plotted in Fig. 4(c) for $I_{dc} = 0$ and $I_{dc} = 1$ mA. The conductivity under modulation is now $\sigma_m^{\text{mod}} = \sigma_m^0 + \Delta\sigma_m$, which is used as an input parameter to model the transport of magnons from injector to detector. Note that we have used $\mu_0 H = 50$ mT, which is larger than the experimental value because our model is only valid in the linear regime (i.e., μ_m smaller than the magnon gap).

The magnon spin diffusion equation is then solved to obtain the chemical potential due to the ac current μ_m^{ac} shown in Fig. 4(d). A significant part of the magnon spin current is absorbed by the modulator, reducing the nonlocal signal in the detector. The model actually overestimates this absorption; from experiments, we observe that roughly 50% of the spin current is absorbed (Supplemental Material [31], Sec. S7). The modulation efficiency η is calculated by finding the spin current into the detector as a function of the dc current. η is plotted in Fig. 4(e) as a function of the sample temperature. It is approximately 3%/mA at 300 K, overestimating the experimentally observed efficiency. While the number of magnons injected via the SHE decreases as the temperature drops, the total number of magnons is also reduced; therefore, the effect of SHE injection on the conductivity is approximately the same. The model predicts a sizeable efficiency at 50 K, which was not observed in our experiments: While the fit yields a negative efficiency at $T = 50$ K, the error is large and includes $\eta = 0$. For $T < 50$ K, we did not observe significant modulation of the nonlocal signal. Note that the experimental data in Fig. 4(e) were obtained from device *G1*, and the comparison to the model is made for the results from the first harmonic signals. However, the modulation efficiencies for the first and second harmonic are of the same order or smaller in devices *G2* and *G3* so that the model predictions in Fig. 4(e) also apply to the measurements on these devices.

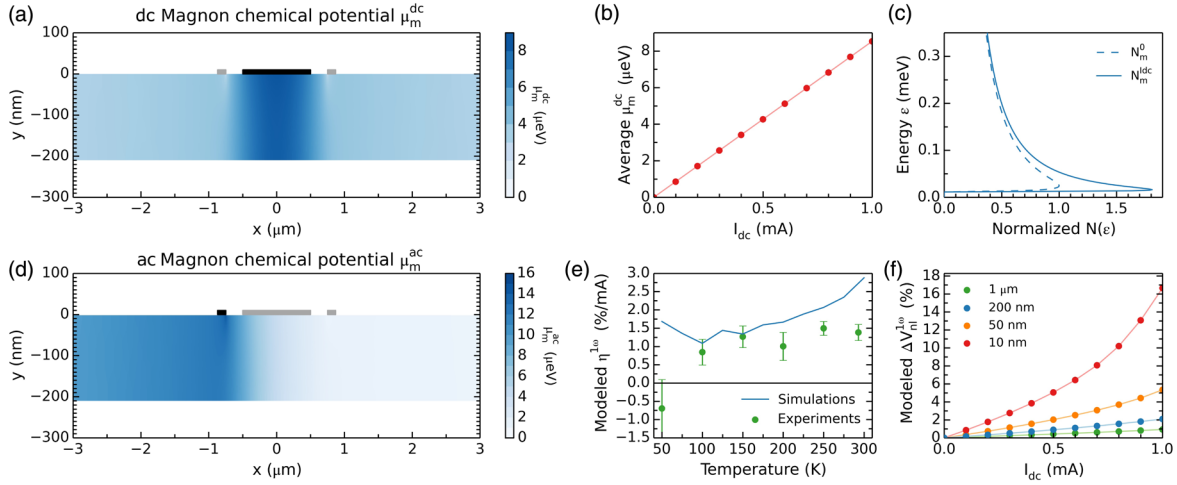


FIG. 4. (a) Magnon chemical potential profile due to the SHE injection of magnons by the dc modulator current. (b) Average magnon chemical potential in the channel as a function of I_{dc} . (c) Low-energy part of the magnon spectral density $N_m = D(\epsilon)f(\mu, T, \epsilon)$ for zero dc current (dashed line) and maximum current (solid line). (d) Magnon chemical potential profile due to the ac injector current. (e) Modulation efficiency as a function of the temperature for a film with $t_{YIG} = 210$ nm. Solid line shows the simulation results; symbols show the experimental results for the first harmonic obtained from sample *G1*. (f) Relative modulation as a function of I_{dc} for various YIG thicknesses.

Figure 4(f) shows theoretical predictions for the relative modulation as a function of I_{dc} for various YIG thicknesses, demonstrating that a larger modulation can be obtained by reducing the thickness. This can be understood since the modulator also acts as a magnon absorber. In thin films, a small change in σ_m will result in a significant change in the spin absorption of the contact. Additionally, reducing the film thickness increases the average μ_m^{dc} since the relaxation of the magnons is suppressed. For $t_{YIG} \leq 50$ nm, a non-linear increase in efficiency can be seen at large currents. Here, the dc magnon chemical potential approaches the magnon gap $\Delta_m \approx E_z$, resulting in a strong increase in the magnon density. Note that possibly related nonlinear effects have recently been observed in nonlocal experiments on extremely thin YIG films [40]. On the other hand, recent studies reported a saturation of μ_m as it approaches the magnon gap [41,42], attributed to the onset of magnon-magnon interactions that suppress population of low-energy states [42,43]. Future experiments should explore thinner YIG films to establish whether the nonlinear regime can be reached.

Summarizing, we observed a dc spin-current-driven modulation of the magnon spin conductance in nonlocal magnon transport experiments in devices consisting of injector, detector, and modulator contacts on YIG films. Via injection of magnons by the modulator, the magnon density and, consequently, the spin conductivity of the channel were modified. Using a finite element model, we explained the efficiency of the modulation effect which we observed. In the modulation of the signal due to electrically generated magnons, an unexpected change of sign as a function of the magnetic field was observed in some but not all devices, which is currently not understood and should be

investigated further. These results pave the way for the development of efficient thermal-magnon-based logic devices.

The authors would like to acknowledge H. M. de Roos, J. G. Holstein, H. Adema, and T. J. Schouten for technical assistance. This work is part of the research program Magnon Spintronics (MSP) No. 159, financed by the Netherlands Organization for Scientific Research (NWO) and supported by NanoLab NL, EU FP7 ICT Grant No. 612759 InSpin and the Zernike Institute for Advanced Materials. R.A.D. is supported by the European Research Council. This research is partly financed by the NWO Spinoza prize awarded to Prof. B.J. van Wees by the Netherlands Organization for Scientific Research (NWO).

*i.j.cornelissen@rug.nl

- [1] W. Shockley, *Proc. IRE* **40**, 1365 (1952).
- [2] V. V. Kruglyak, S. O. Demokritov, and D. Grundler, *J. Phys. D* **43**, 264001 (2010).
- [3] A. A. Serga, A. V. Chumak, and B. Hillebrands, *J. Phys. D* **43**, 264002 (2010).
- [4] A. Khitun, M. Bao, and K. L. Wang, *J. Phys. D* **43**, 264005 (2010).
- [5] M. P. Kostylev, A. A. Serga, T. Schneider, B. Leven, and B. Hillebrands, *Appl. Phys. Lett.* **87**, 153501 (2005).
- [6] A. V. Chumak, V. I. Vasyuchka, A. A. Serga, and B. Hillebrands, *Nat. Phys.* **11**, 453 (2015).
- [7] T. Fischer, M. Kewenig, D. A. Bozhko, A. A. Serga, I. I. Syvorotka, F. Ciubotaru, C. Adelman, B. Hillebrands, and A. V. Chumak, *Appl. Phys. Lett.* **110**, 152401 (2017).

- [8] L. J. Cornelissen, J. Liu, R. A. Duine, J. B. Youssef, and B. J. van Wees, *Nat. Phys.* **11**, 1022 (2015).
- [9] S. T. B. Goennenwein, R. Schlitz, M. Pernpeintner, K. Ganzhorn, M. Althammer, R. Gross, and H. Huebl, *Appl. Phys. Lett.* **107**, 172405 (2015).
- [10] J. Li, Y. Xu, M. Aldosary, C. Tang, Z. Lin, S. Zhang, R. Lake, and J. Shi, *Nat. Commun.* **7**, 10858 (2016).
- [11] H. Wu, C. H. Wan, X. Zhang, Z. H. Yuan, Q. T. Zhang, J. Y. Qin, H. X. Wei, X. F. Han, and S. Zhang, *Phys. Rev. B* **93**, 060403 (2016).
- [12] S. Vélez, A. Bedoya-Pinto, W. Yan, L. E. Hueso, and F. Casanova, *Phys. Rev. B* **94**, 174405 (2016).
- [13] K. Uchida, J. Xiao, H. Adachi, J. Ohe, S. Takahashi, J. Ieda, T. Ota, Y. Kajiwara, H. Umezawa, H. Kawai, G. E. W. Bauer, S. Maekawa, and E. Saitoh, *Nat. Mater.* **9**, 894 (2010).
- [14] G. E. W. Bauer, E. Saitoh, and B. J. van Wees, *Nat. Mater.* **11**, 391 (2012).
- [15] M. Weiler, M. Althammer, F. D. Czeschka, H. Huebl, M. S. Wagner, M. Opel, I. M. Imort, G. Reiss, A. Thomas, R. Gross, and S. T. B. Goennenwein, *Phys. Rev. Lett.* **108**, 106602 (2012).
- [16] J. Xiao, G. E. W. Bauer, K.-i. Uchida, E. Saitoh, and S. Maekawa, *Phys. Rev. B* **81**, 214418 (2010).
- [17] S. M. Rezende, R. L. Rodríguez-Suárez, R. O. Cunha, A. R. Rodrigues, F. L. A. Machado, G. A. Fonseca Guerra, J. C. Lopez Ortiz, and A. Azevedo, *Phys. Rev. B* **89**, 014416 (2014).
- [18] R. A. Duine, A. Brataas, S. A. Bender, and Y. Tserkovnyak, *arXiv:1505.01329v1*.
- [19] L. J. Cornelissen, K. J. H. Peters, G. E. W. Bauer, R. A. Duine, and B. J. van Wees, *Phys. Rev. B* **94**, 014412 (2016).
- [20] J. Shan, L. J. Cornelissen, N. Vlietstra, J. Ben Youssef, T. Kuschel, R. A. Duine, and B. J. van Wees, *Phys. Rev. B* **94**, 174437 (2016).
- [21] K. Ganzhorn, T. Wimmer, J. Cramer, S. Geprägs, R. Gross, M. Kläui, and S. T. B. Goennenwein, *AIP Adv.* **7**, 085102 (2017).
- [22] M. Krawczyk and D. Grundler, *J. Phys. Condens. Matter* **26**, 123202 (2014).
- [23] A. V. Chumak, A. A. Serga, and B. Hillebrands, *Nat. Commun.* **5**, 4700 (2014).
- [24] K. An, D. R. Birt, C. F. Pai, K. Olsson, D. C. Ralph, R. A. Buhrman, and X. Li, *Phys. Rev. B* **89**, 140405(R) (2014).
- [25] O. Gladii, M. Collet, K. Garcia-Hernandez, C. Cheng, S. Xavier, P. Bortolotti, V. Cros, Y. Henry, J. V. Kim, A. Anane, and M. Bailleul, *Appl. Phys. Lett.* **108**, 202407 (2016).
- [26] V. E. Demidov, S. Urazhdin, E. R. J. Edwards, M. D. Stiles, R. D. McMichael, and S. O. Demokritov, *Phys. Rev. Lett.* **107**, 107204 (2011).
- [27] V. E. Demidov, S. Urazhdin, A. B. Rinkevich, G. Reiss, and S. O. Demokritov, *Appl. Phys. Lett.* **104**, 152402 (2014).
- [28] K. Ganzhorn, S. Klingler, T. Wimmer, S. Geprägs, R. Gross, H. Huebl, and S. T. B. Goennenwein, *Appl. Phys. Lett.* **109**, 022405 (2016).
- [29] P. Drude, *Ann. Phys. (Berlin)* **306**, 566 (1900).
- [30] P. Drude, *Ann. Phys. (Berlin)* **308**, 369 (1900).
- [31] See Supplemental Material at <http://link.aps.org/supplemental/10.1103/PhysRevLett.120.097702> for details of the finite element model and additional measurement data obtained from devices G2 and G3, which includes Refs. [32–36].
- [32] G. A. Slack and D. W. Oliver, *Phys. Rev. B* **4**, 592 (1971).
- [33] M. Isasa, E. Villamor, L. E. Hueso, M. Gradhand, and F. Casanova, *Phys. Rev. B* **91**, 024402 (2015).
- [34] S. R. Boona and J. P. Heremans, *Phys. Rev. B* **90**, 064421 (2014).
- [35] S. M. Wu, J. E. Pearson, and A. Bhattacharya, *Phys. Rev. Lett.* **114**, 186602 (2015).
- [36] A. Aqeel, N. Vlietstra, A. Roy, M. Mostovoy, B. J. van Wees, and T. T. M. Palstra, *Phys. Rev. B* **94**, 134418 (2016).
- [37] L. J. Cornelissen, J. Shan, and B. J. van Wees, *Phys. Rev. B* **94**, 180402(R) (2016).
- [38] M. Schreier, G. E. W. Bauer, V. I. Vasyuchka, J. Flipse, K.-i. Uchida, J. Lotze, V. Lauer, A. V. Chumak, A. A. Serga, S. Daimon, T. Kikkawa, E. Saitoh, B. J. van Wees, B. Hillebrands, R. Gross, and S. T. B. Goennenwein, *J. Phys. D* **48**, 025001 (2015).
- [39] L. J. Cornelissen, K. Oyanagi, T. Kikkawa, Z. Qiu, T. Kuschel, G. E. W. Bauer, B. J. van Wees, and E. Saitoh, *Phys. Rev. B* **96**, 104441 (2017).
- [40] N. Thiery, A. Draveny, V. V. Naletov, L. Vila, J. P. Attané, C. Beigné, G. De Loubens, M. Viret, N. Beaulieu, J. B. Youssef, V. E. Demidov, S. O. Demokritov, A. Anane, P. Bortolotti, V. Cros, and O. Klein, *arXiv:1702.05226*.
- [41] C. Du, T. Van der Sar, T. X. Zhou, P. Upadhyaya, F. Casola, H. Zhang, M. C. Onbasli, C. A. Ross, R. L. Walsworth, Y. Tserkovnyak, and A. Yacoby, *Science* **357**, 195 (2017).
- [42] V. E. Demidov, S. Urazhdin, B. Divinskiy, V. D. Bessonov, and A. B. Rinkevich, *Nat. Commun.* **8**, 1579 (2017).
- [43] V. E. Demidov, S. Urazhdin, G. de Loubens, O. Klein, V. Cros, A. Anane, and S. O. Demokritov, *Phys. Rep.* **673**, 1 (2017).